Understanding the role of Ti-rich domains in the stabilization of gold nanoparticles on mesoporous silica-based catalysts

Alaina Moragues [a], Begoña Puértolas [b], Álvaro Mayoral [c,d], Raúl Arenal [c,d], Ana B. Hungría [e], Sonia Murcia-Mascarós [a], Stuart H. Taylor [f], Benjamín Solsona [g,*], Tomás García[b,*], Pedro Amorós [a,*]

[a] Institut de Ciència dels Materials, Universitat de València, P.O. Box 22085, 46071 Valencia, Spain.

[b] Instituto de Carboquímica (ICB-CSIC), C/ Miguel Luesma Castán 4, 50018 Zaragoza, Spain.

[c] Laboratorio de Microscopias Avanzadas (LMA), Instituto de Nanociencia de Aragon (INA), Universidad de Zaragoza, Mariano Esquillor, 50018 Zaragoza, Spain.

[d] Fundación Agencia Aragonesa para la Investigación y el Desarrollo (ARAID), María de Luna 11, 50018 Zaragoza, Spain.

[e] Departamento de Ciencia de Materiales, Ingeniería Metalúrgica y Química Inorgánica, Universidad de Cádiz, Campus Río San Pedro, 11510 Puerto Real, Spain.

[f] Cardiff Catalysis Institute, School of Chemistry, Cardiff University, Main Building, Park Place, CF10 3AT Cardiff, United Kingdom.

[g] Departamento de Ingenieria Quimica, Universitat de València, Avenida de la Universitat, 46071 Valencia, Spain.

*Corresponding authors at: Institut de Ciència dels Materials, Universitat de València, P.O. Box 22085, 46071 Valencia, Spain (Pedro Amorós).

E-mail addresses: pedro.amoros@uv.es, tomas@icb.csic.es, benjamin.solsona@uv.es

ABSTRACT

The preparation and stabilization of gold nanoparticles with a precise control of size and dispersion is highly attractive for a variety of applications, and a key aspect is thermal stability of the nanoparticles. This paper focuses on understanding the effect of TiO_2-based nanodomains, dispersed on mesoporous silicas, and how they control gold nanoparticle stability. The anatase domains have been incorporated through two different strategies: co-hydrolysis of Si and Ti reagents that directly form the mesoporous material through self-assembling with surfactant micelles, or the post-impregnation of the mesosporous silica with $Ti(acac)_2$. Both strategies lead to different incorporation of the anatase domains: partially embedded inside the silica walls, or occupying the mesopores. We have observed that the inclusion in the pores favors the stability of the final material due to a more favorable gold-support interaction and also due to a stabilizing effect associated with a scaffold effect of the anatase crystals, which hinders the collapse of the mesostructure.

Graphical Abstract

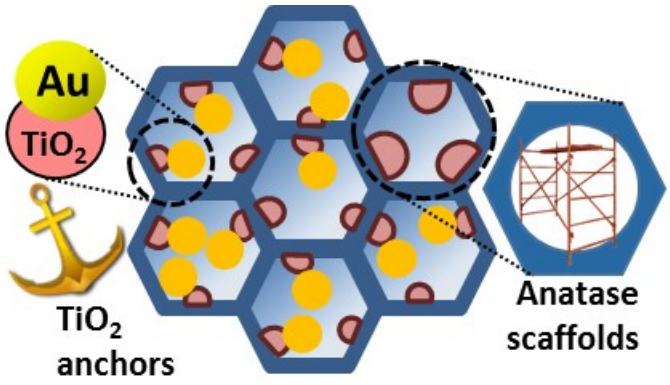

Highlights

- Active gold/anatase/mesoporous silica catalysts for CO oxidation were synthesized
- A high dispersion of gold nanoparticles is achieved even at high temperature
- Anatase domains act as inorganic anchors to stabilize gold nanoparticles
- Anatase domains also acts as scaffold to prevent the mesostructure collapse

Keywords: CO oxidation, gold, nanoparticles, mesoporous silica, anatase

1. Introduction

More than thirty years ago the inactivity of gold as a catalyst was refuted by the independent work of Haruta and Hutchings, who described the importance of supported gold nanoparticles as very active heterogeneous catalysts for low-temperature CO oxidation and ethyne hydrochlorination, respectively [1,2]. Subsequently, the nature and properties of catalysts based on gold nanoparticles have received increased attention due to their superior activity in many industrially and environmentally-friendly important reactions, including selective hydrogenation, epoxidation of alkenes, oxidation of alcohols and Volatile Organic Compounds, coupling reactions and direct H_2O_2 synthesis, amongst others [3-11]. Regardless of the reaction mechanism for each particular process, there is a reasonable consensus on the need for gold particles with a size of less than 10 nm, together with a high particle dispersion [12]. Although gold can coexist as isolated centers, small clusters and nanoparticles, a recent study has shown that, for the oxidation of CO, the conversion rate of nanoparticles is about two orders of magnitude greater than that of isolated atoms [13]. To achieve the desired dispersion of gold a common strategy is the use of supports to control agglomeration and coalescence [2,7,8,11,14].

Generally, the catalytic activity of supported gold nanoparticles is governed by the intimate relationship between the size of the nanoparticle ensemble, the features of the support and the nature of the interface. The decrease of the particle size leads to an increasing proportion of low-coordinated surface atoms [15], together with changes in the electronic properties resulting from the quantum size effect [16,17]. In contrast to non-reducible oxides such as SiO_2, γ-Al_2O_3 or MgO,

supports with redox properties, for example Fe_2O_3, Co_3O_4, Mn_2O_3, CeO_2 or TiO_2, seem to be beneficial for the catalytic activity [18-21]. They can impact the electronic properties of the gold particles and vice versa, by modifying the mechanism of oxygen vacancy formation and replenishment, which enhances the catalyst reactivity.

Together with the intrinsic nature of the support composition, additional aspects related to its morphology and porosity seems to be the key to stabilizing gold nanoparticles. Although SiO_2 may not be the best choice of support specifically for gold nanoparticles, it does have many beneficial properties as a catalyst support. In order to take advantage of the high surface area of mesoporous silicas and their confinement effect inside the mesopores [22], silica can be modified with organic (including periodic mesoporous organosilicas, PMO) and inorganic species to favor the interaction with gold [23-26]. In fact, different metal oxides can be included into the mesoporous silicas. These metal oxides act as inorganic anchors, able to interact with gold precursor species favoring the gold-support interaction [27]. Depending on the chemical nature and crystallinity of the oxidic domains, different environments can be achieved, leading in some cases to strong interfacial interactions when crystalline oxides are present [22,28,29].This last aspect is essential in many industrially and environmentally important reactions.

A challenging problem for the industrial implementation of gold-based catalysts relies on attaining thermally-stable materials under highly demanding operating conditions [30]. In fact, only a few examples exist of supported gold catalysts preserving activity at temperatures higher than 700 ºC. Supported and unsupported metal nanoparticles show rapid particle aggregation, especially at elevated reaction temperatures [31,32], at which the hydrothermal stability of the catalysts becomes a crucial issue [33,34]. Strategies such as post modification of Au/TiO_2 by amorphous SiO_2 decoration [35], the production of core-shell nanostructures [36,37], FeO_x modified hydroxyapatite supported Au catalysts [38], the synthesis of thin porous alumina sheets [39], gold on cobalt oxide particles supported on a mixture of zirconia-based ceria [40], or the formation of complex $Au_2Sr_5O_6$ mixed oxides [41] have been proposed to address this problem. Additionally, the suitability of mesoporous materials, such as M41s or SBA, as matrices to immobilize catalytically active species and provide nano-size confinements inside the pore system has also been reported [42]. However, the lack of thermal stability of nanoparticles on silica supports under severe operating conditions remains a challenge [43]. In fact, even confined inside

mesopores, migration of gold nanoparticles occurs both along the channels and in traverse directions through the silica walls when a SBA-15 silica support is used at temperatures above 550 ºC, according to direct imaging observations [44]. In this regard, we recently proposed gold supported on a TiO_2 impregnated SiO_2 bimodal mesoporous UVM-7 support as a suitable structure to stabilize highly dispersed gold nanoparticles at temperatures as high as 800 °C [45]. The UVM-7 support belongs to the Nanoparticulated Bimodal porous Silicas, in which the decrease of the particle size leads to a shortening of the maximum length of mesopores, together with the generation of a supplementary textural-type inter-particle porosity [46-48]. The dual role of TiO_2 domains as a scaffold [45], preventing the collapse of the SiO_2 mesostructure, and as anchoring islands to avoid gold sintering, are the factors responsible for the stability of gold nanoparticles.

Enticed by the versatility of UVM-7 to be tuned by the incorporation of different metal species in the structure, herein, we synthesize gold-supported TiO_2-containing UVM-7 catalysts via the *one-pot* Atrane route and contrast their properties and performance for CO oxidation, selected as a model reaction, with those previously reported (in which the Ti was incorporated through a second preparative step) [45]. We investigate how the nature and location of Ti-rich domains included in mesoporous silicas impact on stability and activity as heterogeneous gold-containing catalysts. We compare here the influence of the synthesis method (*one-pot* or *two-pot*) and the calcination temperature on the structural organization and activity of the catalyst. Advanced characterization methods including spherical aberration (Cs) corrected scanning transmission electron microscopy, X-Ray photoelectron spectroscopy and ^{29}Si MAS NMR spectroscopy are able to rationalize the impact of the speciation of the TiO_2 domains, and the activation temperature of the catalysts on the stability of the support and gold nanoparticles.

2. Experimental Details

2.1. Chemicals

All the synthesis reagents were analytically pure, and were used as received from Aldrich [tetraethyl-orthosilicate ≥ 98.0 % (TEOS), cetyl-trimethylammonium bromide ≥ 98 % (CTMABr), triethanolamine ≥ 99.0 % (TEA), tetrabutyl-orthotitanate ≥ 98.0 % (TBOT), titanium(IV) oxyacetylacetonate 90 % ($TiO(acac)_2$), potassium tetrachloroaurate(III) 98 % ($KAuCl_4$), sodium hydroxide ≥ 98 % (NaOH) and ethanol].

2.2. Catalyst preparation

Two families of gold containing catalysts, based on the deposition of Au on Ti-modified UVM-7-type mesoporous silicas, were synthesized: Ti-UVM-7 and TiO_2/UVM-7. While the Ti-UVM-7 derivatives were isolated through a *one-pot* method, the TiO_2-UVM-7 catalysts were synthesized through a post functionalization strategy from pure UVM-7 silicas.

Synthesis of UVM-7 pure silica: The synthesis of UVM-7 silica was achieved through the "Atrane route", which combines the use of a cationic surfactant (CTMABr) as a structural directing agent, and consequently as a porogen after template removal, and a complexing polyalcohol (TEA) as hydrolysis retarding agent [49]. The molar ratio of the reagents was; 2 TEOS:7 TEA:0.52 CTMABr:180 H_2O [46,47]. In a typical synthesis, the corresponding amounts of TEOS (10.7 mL) and TEA (22.3 mL) were mixed under continuous stirring at 140 ºC until a homogeneous dispersion was achieved. The temperature was then decreased to 120 ºC and the CTMABr (4.23 g) added. The resulting gel was cooled to 80 ºC and distilled water (80 mL) was added. This mixture was aged at room temperature for 16 hours under continuous stirring. The resulting mesostructured powder was separated by filtration, washed extensively with deionized water and ethanol, and dried at 60 ºC for 16 hours. In order to prepare the final porous material, the template was removed by calcination at 550 ºC for 6 hours (heating ramp = 5 ºC/min) under static air atmosphere. A sample of the pure silica UVM-7 was calcined at 800 ° C for comparative purposes, and was labeled as UVM-7 800.

Synthesis of Ti-UVM-7: Titanium was included into the UVM-7 following a co-condensation method: the titanium precursor (TBOT) was included in the first step of the UVM-7 synthesis to obtain a mixture of atrane complexes (Si and Ti), and then the protocol was the same as for UVM-7 [50]. The Ti content can be modulated between Si/Ti= ∞ to Si/Ti=1 starting from the 2-xTEOS:x TBOT:7 TEA:0.52 CTMABr:180 H_2O molar ratio. In this work we synthesized four supports with nominal Si/Ti values of 21, 5, 4 and 1 that have been denoted as Tix-UVM-7(1)RT (x = 22, 5, 4 and 1; (1) indicates *one-pot* synthesis).

Synthesis of TiO_2/UVM-7: The titanium incorporation was carried out through a wet-impregnation procedure, previously described by Narkhede *et al* [51]. The corresponding weight of $TiO(acac)_2$ was dissolved in 100 mL of pure ethanol. Deionized water was slowly added while continuous vigorous stirring. Subsequently, the impregnation of the calcined UVM-7 silica support (0.6 g) was carried out by stirring the sample for 2 hours with the Ti solution. The mixture was

filtered and washed thoroughly. The cake was allowed to dry for 16 hours at room temperature and the TiO_2/UVM-7 was calcined in static air atmosphere at 300 ºC for 5 hours with a heating rate of 1 ºC/min. Four different nominal titanium loadings were tested: Si/Ti= 21, 5, 4 and 1, that have been denoted as Tix-UVM-7(2)RT (x= 21, 5, 4 and 1; (2) indicates *two-pot* synthesis).

For comparative purposes, some supports were calcined at 400ºC and 800ºC and labelled as Tix-UVM-7(Y)CT (Y= 1 or 2; CT= 400ºC or 800ºC).

Synthesis of Au/Ti-UVM-7 and Au/TiO_2/UVM-7: The gold incorporation onto both supports was performed by the conventional deposition-precipitation technique [51,52]. 43.4 cm^3 of an aqueous solution ($5.078 \cdot 10^{-3}$ M) of $KAuCl_4$ were heated at 70 ºC in a water bath wrapped by an aluminum foil to exclude light. The initial pH was around 2.5. It was carefully adjusted to pH=8 by dropwise addition of a 0.1 M aqueous solution of NaOH. The pH was maintained around 7 for 30 minutes. 0.5 g of the required support was then added and pH adjusted (7-8) into the acidic region, controlled by adding NaOH. After the pH was constant for 15 minutes, the suspension was stirred for another hour at the same temperature. Finally, the suspension was cooled, filtered and washed with deionized water. The resulting cake was heated at 90 ºC for 13 hours. After the preparation, the samples were stored in the dark in a vacuum desiccator at room temperature. Each sample was divided into three portions: the first portion was kept uncalcined; the second portion was calcined at 400 ºC in static air for 4 hours with a heating rate of 1 ºC/min and the third one was calcined at 800 ºC in static air under the same conditions. In all cases, the final catalysts were stored in a vacuum desiccator at room temperature. The samples are coded Au-Tix-UVM-7(Y)CT, where x represents the Si/Ti molar ratio, Y the method (1 for co-condensation, *one-pot*, and 2 for impregnation, *two-pot*) and CT stands for the calcination temperature (RT, 400 or 800). Tables 1 and 2 summarize the main synthesis variables and physical data.

Synthesis of Au/TiO_2/MCM-41: A catalyst based on a MCM-41 support was also synthesized for comparative purposes. The MCM-41 pure silica has been synthesized in a similar way as the UVM-7 silica, starting from silatrane as the hydrolytic precursor. Later, we incorporated the Ti species by using the *two-pot* protocol by using $TiO(acac)_2$ as precursor. Finally we added the gold through a conventional deposition-precipitation technique. We have used a nomenclature analogous to the previous one: Au-Tix-MCM-41(Y)CT. The final catalyst with a Si/Ti= 6 molar ratio is labelled as Au-Ti6-MCM-41(2)RT, and the calcined samples as Au-Ti6-MCM-41(2)400 and Au-Ti6-MCM-41(2)800.

2.3.Characterization

The titanium and gold contents were determined by energy dispersive X-ray spectroscopy EDX analysis using a Scanning Electron Microscope (Philips - SEM-XL 30). Si/Ti and Si/Au molar ratio values averaged from EDX data corresponding to *ca.* 50 different particles of each sample were used. Powder X-ray diffraction (XRD) was carried out using a Bruker D8 Advance diffractometer with monochromatic Cu Kα source operated at 40 kV and 40 mA. Patterns were collected in steps of 0.1º(2θ) over the angular range 1.5-10.0 º(2θ) for 10 s per step. Additionally, XRD patterns at high-angle values were also recorded. For electron microscopy analyses, the samples were dispersed in ethanol and placed onto a carbon coated copper microgrid and left to dry before observation. Spherical aberration (Cs) corrected scanning transmission electron microscopy high-angle annular field (STEM-HAADF) imaging analyses were performed in a XFEG FEI Titan microscope operated at 300 kV. The microscope was equipped with a CEOS aberration corrector for the electron probe, achieving a point resolution of 0.8 Å, an EDAX EDS detector and Gatan Energy Filter Tridiem HR865 for electron energy loss spectroscopy (EELS). These spectroscopic data were obtained using the spectrum-image acquisition mode [53,54]. The textural characterization of the samples was carried out by N_2 adsorption at -196 ºC, using a Micromeritics ASAP 2020 apparatus. Prior to the adsorption measurements, the samples were outgassed in situ in vacuum at 120 ºC for 15 hours to remove adsorbed gases. Surface areas were calculated from nitrogen adsorption isotherms in the relative pressure range from 0.1 to 0.25 using the BET equation (S_{BET}). Both BJH pore size distributions and volumes were obtained from the adsorption branch of the N_2 adsorption isotherms. X-Ray Photoelectron Spectroscopy (XPS) measurements were made on an Omicron ESCA+ photoelectron spectrometer using a non-monochromatized MgKα X-Ray source (hν = 1253.6 eV). Analyzer pass energy of 50 eV was used for survey scans and 20 eV for detailed scans. Binding energies were referenced to the C1s peak from adventitious carbonaceous contamination, assumed to have a binding energy of 284.5 eV. Raman spectra were obtained using a HORIBA Jobin Yvon iHR320 spectrometer with Peltier-cooled CCD and a 532 nm and 785 nm doubled YAG laser excitation source. ^{29}Si MAS NMR spectra were recorded on a Varian Unity 300 spectrometer operating at 79.5 MHz, with a magic angle spinning speed of at least 4.0 kHz.

2.4. Catalytic testing

CO oxidation was used as a model reaction in order to derive property-function relationships. CO catalytic oxidation was performed at atmospheric pressure and at a temperature of 20 ºC, using a fixed bed reactor with an inner diameter of 5.8 mm. A mixture of 0.4 % v/v CO, 20 % v/v O_2 and argon balance was passed through a 10 mg fixed bed of catalyst with a flow rate of 100 cm^3/min, which corresponded to a space velocity of 600,000 $cm^3/(g_{cat} \cdot h)$. Analyses were performed by an on-line gas chromatograph (Varian CP-3800) with a thermal conductivity detector. The conversion of CO and the formation of CO_2 were both quantified, which led us to measure a carbon balance with and accuracy of ± 2%. After being used in the reactor, the catalysts were stored at room-temperature in a vacuum desiccator before spectroscopic analysis.

3. Results and discussion

3.1.Synthesis of the porous silica support

Porous nature, composition and dispersion of the active sites are key parameters to control the activity of a heterogeneous catalyst. Our first selection concerns the porosity of the support. Accordingly, we decided to use hierarchical porous silicas of the UVM-7 type [48]. This material displays an enhanced accessibility when compared to classical unimodal mesoporous silicas [48]. The most important parameter for the preparation of this material is the pH, that must be in the 8-9 range [46,47]. From the procedural point of view, this value is easily achieved by using TEA as reagent. TEA has a double role, as chelating ligand to form atrane complexes (see below), and as a buffer (pH ca. 8-9). Under these pH conditions, the hydrolysis and condensation of the silica species are favored (leading to the nucleation of primary nanoparticles)[55] but the re-dissolution is greatly hindered, strongly limiting the particle growth.

3.2. Preparative strategies for Ti incorporation

In order to optimize the catalyst compositions, two series of UVM-7 type mesoporous silica-based supports containing a variable proportion of Ti were synthesized. The principal difference between these silica supports resides in the way in which the Ti-species have been incorporated: through *one pot* or by post impregnation (*two-pot*) methods. In the first method, Ti was incorporated through co-hydrolysis and co-condensation with the silica species. We used the well-established atrane route that uses metal (Ti) or metalloid (Si) complexes containing ligands derived

from triethanolamine as hydrolytic inorganic precursors. In this case, a mixture of Si-atrane (silatrane) and Ti-atrane (titanatrane) complexes were used. In general, the atrane complexes are thermodynamically unstable, but kinetically inert when they react with water. The result is more closely matched reaction rates when compared with a mixture of commercial alkoxides, avoiding significant phase segregation of Ti and Si oxides. The Ti incorporation and the self-assembly with the CTAB micelles occur simultaneously, and consequently the inorganic functionalization of the mesoporous walls and the mesopore formation are achieved in a single step. Hence, mesoporous solids with an intimate mixture of the two heteroelements can be obtained through this method, due to the presence of CTAB micelles as porogen species.

We have used EDX, not only to determine the amounts of Ti incorporated to the framework, but also to check the chemical homogeneity of the resulting solids. Si/Ti molar ratios are summarized in Table 1. EDX data indicate that the reported Ti-UVM-7 materials (Tix-UVM-7(1)) have a high chemical homogeneity, with a regular dispersion of Ti along the mesopore walls. Additionally, it is observed that the measured final titanium content is slightly higher than the nominal one. While Ti is completely removed from the starting mother solution due to the formation of oxidic nanodomains, a certain proportion of Si-based oligomers remain as soluble species in equilibrium with the silica [55]. This leads to a certain (indirect) enrichment in titanium.

The second *two-pot* method is based on a simple wet impregnation of UVM-7 pure silica with $TiO(acac)_2$. In this case, the inclusion of the Ti species occurs on the surface of the mesopore walls. We have selected $Ti(acac)_2$ as the source of Ti, due to the fact that this compound shows a melting point (184ºC) lower than its decomposition temperature (>210ºC). This implies a homogeneous dispersion of the compound on the silica surface can be achieved prior to its decomposition to produce TiO_2, obtaining a better dispersion from impregnation than with other Ti sources. The EDX analysis confirms the preservation of a high dispersion of Ti at a micrometric level (spot size of 1μm). In comparison with the *one-pot* method (Table 1), the relationship between the nominal and measured Ti content followed the reverse trend to the *one-pot* synthesis. Measured Ti content was slightly lower than the nominal one. This fact is probably related to the preparation protocol, since intensive washing was carried out in the final step prior to the thermal treatment, and this may remove some Ti.

3.3. Gold deposition

A deposition-precipitation method is one of the most convenient procedures for adding gold nanoparticles onto metal oxide supports, such as TiO_2 [56]. Gold was added to both Ti-containing UVM-7 supports following a deposition-precipitation technique in aqueous $KAuCl_4$ solutions at pH 7-8. Under this condition, $Au(OH)_4^-$ species are dominant [57]. The low isoelectric point of the silica surface (*ca.* 2–3) strongly hinders the interaction with an anionic species [55]. $Au(OH)_4^-$ complexes require a positively charged surface, and this is provided by the TiO_x anchoring nanodomains, having a *zero point charge* around 6, which varies over the range 3.9–8.2, depending on factors like particle size and degree of hydroxylation [56,58]. Moreover, at the working pH, other mechanisms have been proposed based on the interaction of $Au(OH)_3{\cdot}H_2O$ neutral species on Ti-OH centers at the anatase surface [59,60]. Au complexes will interact in a preferred way with the Ti-rich nanodomains, partially embedded inside the mesopore walls (*one-pot* method; see below) or formed on the surface (*two-pot* method), rather than with the pure silica surface. The resulting homogeneity and dispersion of gold particles will reflect those achieved for TiO_x-based inorganic anchors. The gold deposition procedure does not alter the Ti content (Table 1). The amount of gold incorporated increases with the the increase of titanium, regardless of the method used for the addition of Ti-containing nanodomains (i.e. one or *two-pot* synthesis), up to the Si/Ti=5 nominal molar ratio. This fact supports the role of Ti nanodomains as inorganic anchoring points for gold. Nevertheless, in both series we observe an appreciable decrease of the gold content for the materials with the highest Ti content. This fact is due to the qualitative changes affecting the support porosity for the highest Ti samples. In the case of the solids synthesized trough the Atrane route, for samples having Si/Ti molar ratio close to 1, an abrupt decrease in surface area and pore volume occurs, which implies major loss of the porous nature. Consequently, the decrease of accessible Ti-containing nanodomains leads to lower gold incorporation. On the other hand, for the supports prepared through the *two-pot* method, the gold content also decreased for the highest Ti-containing sample. This can be explained considering that both pore volume and accessibility also decrease; this decrease is likely to be related to an increasing amount of TiO_2 crystals formed inside the mesopores (leading to pore necking or even blocking). Nevertheless, the *two-pot* method seems to be more efficient for the gold incorporation. At this point, at least two factors must be considered: the accessibility and the nature of the Ti-containing nanodomains. Whilst in the *two-pot* method all of the Ti species are located in the pores, with all the surface accessible for gold

deposition, in the *one-pot* route only a part of the surface is able to interact with gold complexes. Additionally, a bigger size of the TiO_2 domains formed through the *two-pot* method is expected, due to the lower restrictions to crystal growth when compared to the domains partially or completely embedded inside the walls (*one-pot*).

3.4. Catalytic model

In order to limit the number of samples to be used in the catalytic tests, we have used an empirical approach: uncalcined catalysts with different Ti content were tested at ambient temperature for CO oxidation. In both series, samples with Si/Ti real molar ratio = 4 were found to be the optimal, as shown in Figure 1, and the study focused on these catalysts. In Figure 2 catalytic activity of materials prepared by both methods is shown. For both families, we compared catalysts processed under three different conditions: uncalcined, and treated in air at 400 and 800ºC. For comparison, our uncalcined catalysts (but treated at 90ºC during long time to favor the reduction of $Au(OH)_4^-$ and $Au(OH)_3{\cdot}H_2O$ species) show similar or much better conversion values for CO oxidation than the Au/TiO_2 from the World Gold Council (WGC) (*ca.* 34% under the same conditions). When both catalyst series are compared, it is evident that better activity is achieved for catalysts in which the Ti species were introduced through impregnation (*two-pot*). *One-pot* catalysts present lower conversion, even for uncalcined materials, although they were stable with time. In contrast, the *two-pot* uncalcined catalyst presents higher conversion, but it decreased with time-on-line. It should be highlighted that activity stabilized when samples were calcined, and showed high conversion.

Au-Tix-MCM-41 catalysts were also evaluated for comparative purposes. The catalytic results justified our selection of support. For a similar Ti and Au content, the catalytic data for unimodal MCM-41 silica support was significantly poorer when compared to the respective UVM-7 type materials (Figure S1). The decreasing CO conversion with time is more pronounced for MCM-41 derived catalysts, and is even more significant for those calcined. The relatively lower accessibility for the 1-D porosity of MCM-41, when compared to the open architecture of 3-D UVM-7, is a disadvantage on a number of different levels. Firstly, during the synthesis, a poorer distribution of $TiO(acac)_2$ by impregnation is anticipated and consequently lower homogeneity of Ti-nanodomains is expected for MCM-41 and, in turn, poorer gold dispersion. Secondly, catalysis can be effected due to both lower and more restricted accessibility of the substrates to the active

sites. These advantages of UVM-7 type supports for catalytic applications have already been demonstrated in a number of previous studies [45,61].

3.5.Materials characterization

It is well accepted that in order to obtain notable catalytic results in terms of activity and stability, the active gold nanoparticles must be relatively small and well dispersed over the support [62], and these sites must be fully accessible even after treatments using severe high temperature conditions. At this point, HAADF images in Figure 3 are of special significance to compare our catalysts. In all cases, including used catalysts, we observe a high homogeneity and dispersion of the gold nanoparticles. Undoubtedly, there is a beneficial effect obtained from the presence of Ti species in the support. In the absence of Ti, the inclusion of gold under the same preparative conditions (Si/Au= 127) results in catalysts that display an important lack of homogeneity and dispersion of the active species (Figure S2). Moreover, we observe a significant growth of the gold nanoparticles, which increase even more after calcination at 800ºC. In conclusion, and as previously stated, the presence of Ti favors the gold nanoparticle distribution in an optimal way.

At micrometric scale, the mapping of the distribution of the Ti and Au shows the regular distribution of both elements, allowing us to discard phase segregation phenomena at a relatively large-scale, independently of the Ti incorporation procedure used (Figure S3). In addition, dispersion of titania and gold has been studied by spherical aberration (Cs) corrected scanning transmission electron microscopy high-angle annular field (STEM-HAADF). Figures 4 and 5 compare Au/Ti-UVM-7 materials prepared in *one-pot* synthesis before and after calcination. In both cases, a high dispersion of Ti is observed. In the uncalcined sample, Ti is distributed in Ti-rich nanodomains of *ca.* < 4 nm and, moreover, a certain amount of titanium seems to be highly dispersed, probably in the form of small oligomers (according to the observation of extremely small orange spots in the mapping figure). After heating up to 800 ºC, the high Ti dispersion is maintained, but the well-defined pseudo-spherical form of the Ti-rich domains is lost. This evolution is probably due to the Si-Ti inter-diffusion at high temperature. Despite the similarity of the Ti dispersion before and after calcination, a slight gold particle sintering was detected, increasing from 5.9±2.5 nm (uncalcined) to 6.3±2.0 nm (T= 400ºC), and 7.7±1.9 nm (T= 800 ºC). This marginal growth in the gold particle size does not seem to be responsible for the decreasing activity. Indeed, the low size of gold particles obtained in the case of Au-Ti5-UVM-7(1)800 can

be considered a priori and unexpected if we take into account that the final catalyst was calcined at a high temperature of 800 ºC. The thermal stability of metal nanoparticles is closely related to their mobility on the support during the thermal treatment. When Hüttig temperature ($T_{Hüttig}$= 0.3 T_M = 128 ºC for gold) is reached, atoms at defects and surfaces will become mobile [63]. The atomic mobility strongly increases, affecting bulk atoms when the treatment temperature is higher than the Tammann temperature ($T_{Tammann}$ = 0.5 T_M = 395 ºC for gold), with the subsequent agglomeration or sintering phenomena. Moreover, the melting point of gold nanoparticles decreases drastically with decreasing particle size (T_M < 300 ºC for particles around 5-6 nm), as well as Hüttig and Tammann temperatures [22]. Hence, for gold particle sizes around 6 nm, Hüttig and Tammann temperatures of ca. 90ºC and 150ºC can be estimated. Therefore, although a certain gold particle mobility and subsequent growth by sintering is favored under these high temperatures, the presence of Ti-rich domains act as inorganic anchoring region and seems to perform a key role in the thermal stabilization of the gold nanoparticles.

The paramount importance of the Ti-domains in the stabilization of the gold nanoparticles is more evident when we compare the behavior of the catalysts synthesized through the *one-pot* and the *two-pot* strategies. In previous work we analyzed in detail the structure and activity of the Au/TiO_2-UVM-7 sample calcined at 800 ºC [45]. In this catalyst family, no growth of the gold nanoparticles was detected after the heat treatment, sizes remained unaltered: 3.7±1.6 nm (uncalcined) and 3.5±1.6 nm (T = 800 ºC) (Figure 6). It should be pointed out that the differences found in the particle sizes between *one-pot* and *two-pot* strategies could contribute strongly to the higher catalytic activity of the *two-pot* sample, although to a lower extent for the uncalcined samples. However, considering the catalytic activities obtained the differences of gold particle size cannot be considered as the only factor controlling the performance of these catalysts.

Since gold nanoparticles are mainly deposited into the mesoporous UVM-7 structure, the accessibility of the reactants to the active sites is another important parameter to be taken into account. In line with this, the evolution of the support porosity after heat treatment was assessed. The general UVM-7-type morphology, based on the presence of nanoparticle clusters, seems to be preserved for all catalysts according to TEM images (Figure 7). We clearly observe the conservation of the large inter-particle meso/macro-porosity. However, the intra-particle mesoporosity seems to be, at least, partially lost or strongly affected in the catalysts heated to 800 ºC. On the contrary, the typical (and partially well ordered) light contrast white regions, associated

with the intra-particle mesopores can be identified in an unambiguous way for uncalcined and catalysts treated at 400 ºC. Moreover, in all cases we observe high contrast very dark regions due to the gold nanoparticles.

Low-angle XRD patterns confirm the evolution of the intraparticle mesostructure with temperature (Figure 8). Regardless of the method used (*one-pot* or *two-pot*), the Au-free supports present diffraction patterns with an intense and large signal at low angles that can be associated with the (100) reflection, assuming the existence of a pseudo-hexagonal cell that occurs in MCM-41 silica (in fact, the UVM-7 silica could be considered as a nanometric and disordered version of the MCM-41) [64]. This signal, that indicates the existence of a partially ordered mesostructure, diminishes in intensity or evolves towards a shoulder peak, after incorporation of gold. This evolution is consistent with a loss of contrast as Au species are included inside the mesopores. This signal is preserved for samples calcined at 400 ºC. However, in the case of the samples heated at 800 ºC, this signal practically disappears, and this is in good accordance with the previous TEM images.

The changes in the mesostructure can also be understood and quantified through analysis of the N_2 adsorption-desorption isotherms (Figure 9). The second nitrogen adsorption step at high P/P_0 pressures is preserved in all cases. The presence of a more marked H1 hysteresis loop for samples isolated through the *two-pot* method is probably due to a pore necking effect of TiO_2 nanodomains inside the mesopores, instead of a more regular distribution of Ti-rich domains partially embedded in the silica walls. On the contrary, the first adsorption step, at intermediate P/P_0 values, only remains for samples heated up to 400 ºC (Table 2). This indicates that the intra-particle mesopores persist at 400 ºC, whilst they collapse appreciably at 800 ºC. This effect is in line with the evolution of the BET surface areas, that remain higher (> 700 m^2/g) for uncalcined samples or solids treated at 400 ºC, but significantly decreased when catalysts are processed at 800 ºC. This effect was more relevant for the *one-pot* prepared sample. Thus, whilst BET surface area for the *one-pot* sample calcined at 800 ºC was decreased to 55 m^2/g, the impregnated one conserves a remarkable value of 245 m^2/g. It is worth pointing out that despite the partial collapse of the UVM-7 structure, the surface area values preserved are still relevant from a catalytic point of view and, therefore, need to be carefully evaluated. Accordingly, the evolution of the mesoporosity of the samples after the heat treatments was evaluated by measuring the BJH pore size distribution. Figure 10 shows a small tail in the border region between micro and mesoporosity for the Au-Ti5-UVM-7(2)800

sample that suggests nitrogen adsorption for small meso and/or micropores. Conversely, the BJH distribution in the case of the Au-Ti5-UVM-7(1)800 catalyst curve in the 1.7-4 nm range is almost flat, which suggests a larger mesostructure collapse. Since the presence of some microporosity was suggested, a DFT analysis was carried out. Figure 11 again shows a partial preservation of the mesoporosity for Au-Ti5-UVM-7(2)800 and Au-Ti5-UVM-7(1)800 samples, and it was significantly more important in the case of the sample synthesized through the *two-pot* method. Additionally, the DFT pore size distribution curves show the presence of a peak in the microporous range (size < 2 nm), associated with a differential pore volume of 0.11 and 0.34 cm^3/g for Au-Ti5-UVM-7(1)800 and Au-Ti5-UVM-7(2)800 samples, respectively. In order to understand the factor responsible for this residual porosity, Figure 11 shows the DFT pore distribution curves for both catalysts (*one* and *two-pot*) at different preparative stages (before and after Au incorporation), and the UVM-7 pure silica for comparative purposes (all heated at 800ºC). The residual microporosity is really scarce for the UVM-7 silica (*ca.* 0.05 cm^3/g), as the intraparticle mesopore system is lost after calcination at 800ºC. The catalyst prepared through the Atrane route shows a similar microporosity (0.09 cm^3/g), and it is slightly higher for the final gold-containing sample. Interestingly, this microporosity increases in an appreciable way in the case of the *two-pot* prepared catalyst, both before and after gold incorporation. This residual micro/mesoporosity, due to a partial mesostructure collapse, combined with the interparticle macroporosity, could also be linked to the higher catalytic activity showed by Au-Ti5-UVM-7(2)800 catalyst, when compared to the activity of Au-Ti5-UVM-7(1)800 material, since a lower accessibility to the gold nanoparticles located at the internal particle surface after the partial mesostructure collapse could lead to an important loss of available active sites. Therefore, it can be stated that there is a direct relationship between the catalytic performance and the preparative chemistry route. Accordingly a higher thermal stability is observed when the TiO_2 nanodomains are located inside the void mesopores (through impregnation), rather than when inclusion occurs inside the mesopore walls (by the Atrane route). It can be postulated that a scaffold effect is attributed to the TiO_2 species impregnated in the mesopores, enhancing the stability of the UVM-7 support. In addition, we observe that the presence of gold nanoparticles cooperates to favor a certain microporosity, when compared to the gold-free samples. The gold nanoparticles also potentially enhance the scaffold effect of the TiO_2 domains.

The different thermal stability of the gold nanoparticles seems to be linked to the crystallinity and/or nature of the Ti-containing domains. Laser Raman spectroscopy (Figures 12 and 13) confirms anatase as the predominant crystalline phase for all catalysts synthesized through the *two-pot* method, regardless of the final temperature treatment. Peaks observed at *ca.* 150, 200, 400, 516 and 640 cm^{-1} can be assigned to E_g, E_g, B_{1g}, A_{1g} and E_g anatase Raman modes, respectively [65]. It is remarkable that even for the non-calcined material, low intensity, but clear signals assignable to anatase can be observed. The signal intensities increased with the increase of processing temperature. For samples treated at lower temperatures (RT and 400 ºC) the peak at 196 cm^{-1} almost disappeared, whilst the 397, 513 and 635 cm^{-1} peaks (from the anatase phase) blue-shift to 402, 519 and 640 cm^{-1} (sample heated at 400 ºC), and to 401, 517 and 637 cm^{-1} (uncalcined sample). Simultaneously, the low frequency E_g peak also blue-shifts from 139 cm^{-1} (anatase) to *ca.* 150 cm^{-1} (148 and 151 cm^{-1} for samples calcined at 400ºC and uncalcined, respectively), and it is broadened asymmetrically. According to the literature this evolution suggests the existence of small anatase crystals with sizes lower than 3-4 nm as predominant domains [65,66]. In the case of the catalyst calcined at 800 ºC, the clear presence of all the signals, as occurs in the anatase reference phase, and the lower blue-shift observed correlates with the growth of the anatase domains to sizes of *ca.* 7 nm. HRTEM images (Figure S4) confirm the maximum anatase particle sizes inferred from Raman [65,66].

On the contrary, for catalysts prepared by the *one-pot* method, only in the case of the solid calcined at 800ºC all the anatase phase Raman signals were unequivocally observed (Figure 13). Even for this last sample, the observed blue-shifts, signal intensities and broadening were consistent with the existence of very small anatase domains (< 3 nm) [65,66]. When catalysts are calcined at lower temperatures, the intense and characteristic anatase low-frequency signal at 143 cm^{-1} disappears. New low intensity and broad signals at *ca.* 480 and 965 cm^{-1} were detected. These peaks can be attributed to vibrations of Si-O-Si and Si-O-Ti linkages, similar to those that occur in the case of silicotitanates [67-69]. Probably, the Atrane method leads to Ti-rich domains more similar to silicotitanates than to anatase when relatively low calcination temperatures are used. Regardless of the crystalline phase formed; anatase, rutile or silicotitanate, the small crystallite size is consistent with the absence of diffraction peaks in the high-angle pattern (Figure 8).

Whilst anatase crystals seem to generate a preferred interaction with gold nanoparticles through a strong interfacial anchoring [20,29], this favorable effect is diminished for titanosilicate domains,

and in a more significant manner for pure silica surfaces, where the amorphous nature and unfavorable isoelectric point suggest that a strong interaction does not take place. These differences (affecting the gold-support interaction) for catalysts synthesized through *one* and *two-pot* strategies could be responsible for the comparatively larger gold particle sizes observed in the materials obtained by using the Atrane route.

The comparative analysis of the ^{29}Si NMR spectra recorded for calcined and uncalcined samples allows us to make a rough estimation about the percentage of anatase and titanosilicate domains and to propose the evolution of these domains with the temperature (Table 3 and Figure S5). In our previous work, centered on the catalyst isolated through impregnation and processed at 800 ºC, we concluded that 62% of titanium evolved to anatase domains, whilst 38% was dispersed by inter-diffusion inside the silica walls [45]. In the case of the *two-pot* preparative strategy a partial migration of Ti occurs from the pore surface to the inside of the silica walls as the temperature increased. However, a contrary effect was followed by titanium for catalysts prepared through the Atrane route. A comparison of the ^{29}Si NMR spectra of the Si-Ti supports, Ti5-UVM-7(1)RT and Ti5-UVM-7(1)800, and a Ti-free UVM-7 silica calcined at 800 ºC are shown in Figure S5. As the temperature increases from 550 ºC up to 800 ºC, the relative intensity of signals at *ca.* -100 and -90 ppm decreased, whilst the signal at *ca.* -110 ppm increased. Taking into account that changes in the amount of silanol groups after treatment at these temperatures must be small, we can assign the signal intensity to evolution of different proportions of Si(4Si), Si(3Si,1Ti) and Si(2Si,2Ti) sites, that show typical chemical shifts at -110, -100 and -90 ppm, respectively [70-72]. From data in Table 3, it is possible to estimate a decrease of *ca.* 14% in the proportion of titanosilicate nanodomains. This implies some diffusion of Ti from titanosilicate sites to TiO_2 through the formation of Ti-oligomers. This evolution is in good agreement with conclusions based on the changes observed in the Raman spectra.

From comparison of the ^{29}Si NMR spectra of Ti5-UVM-7(1)800 and the calcined UVM-7 silica (Figure S5 and Table 3) it is possible to estimate the proportions of anatase and titanosilicate domains. In the case of the Si-Ti support synthesized by co-condensation (*one-pot*), similar proportions of anatase (60%) and titanosilicate (40%) domains are present for the catalyst calcined at 800 ºC. The lower proportion of anatase, when compared to the catalyst synthesized through impregnation (72%), is in good agreement with Raman studies, in which anatase signals with comparatively lower intensity were observed for products obtained by *one-pot* co-condensation.

The higher proportion and size of the anatase domains in the case of the TiO_2/UVM-7 support, together with the location of these crystals inside the mesopores are factors that contribute in a synergic way, to both a stronger gold-support interaction leading to smaller gold nanoparticles, and a better scaffold effect with the subsequent improvement in the thermal stability.

Finally, since it cannot be discounted that there could be an influence on the catalytic performance due to a variation of the gold surface oxidation state, the oxidation state of gold on the surface of the nanoparticles was investigated using X-ray Photoelectron Spectroscopy (XPS). The uncalcined catalyst has some cationic gold, ($Au^{\delta+}/Au^0 = 0.24$), which is preserved after heating at 400 ºC ($Au^{\delta+}/Au^0 = 0.24$), whilst only metallic gold is present after heat treatment at 800 ºC. Considering gold oxidation state, no differences were detected for both series of catalysts, synthesized by *one*- or *two-pot* methodologies, and the changes are only due to the process temperature. Therefore, the role of the gold oxidation state on the catalytic performance can be neglected.

4. Conclusions

In our catalysts the active sites are the gold nanoparticles and there is a close correlation between activity and particle size (Figure 14a). Gold on titania containing UVM-7 siliceous materials were prepared by two different procedures (*one-pot* and *two-pot*), and in both cases it was observed that the calcination at high temperature (800 ºC) does not lead to the formation of large gold particles, since it has been observed that the average gold particle size never exceeds 8 nm. However, some important differences were apparent between the materials prepared using the two methods. By using the *two-pot* impregnation method the gold particle size is very small in all cases and it is unexpected, as it is unaltered by changes in the calcination temperature (Figure 14a). On the contrary, in the case of the *one-pot* Atrane method, slightly larger gold particle dimensions are obtained, and progressive gold particle growth is detected as the calcination temperature increases (and especially when heating to 800ºC). The maximum size differences between the two methods does not exceed a factor of 2. When both preparation methods were compared and no differences were detected for the intrinsic nature of the gold particles; the Au^0 species are dominant. However, these are not the only relevant parameters. For a similar UVM-7-type support architecture, the nature of the Ti-containing domains plays a key role in helping to understand the activity differences between both families. In the case of uncalcined or samples treated 400 ºC, Ti domains

are in the form of titanosilicate or anatase for catalysts synthesized by *one-pot* or *two-pot* methods. The presence of anatase domains probably favors a strong interfacial anchoring effect that prevents gold sintering. At higher temperatures, the sudden decrease of the catalytic activity in the case of the *one-pot* catalysts can be attributed to the complete collapse of the mesostructure, with the subsequent accessibility loss (Figure 14b). This does not occur for the *two-pot* catalysts, in which the larger proportion of anatase crystals located in the mesoporous voids act as a scaffold, hindering the UVM-7 mesostructure collapse. In this last case a good correlation between the CO conversion and the surface area (Figure 14b,) is observed.

Acknowledgments

This research was supported by the Spanish Ministerio de Economia y Competitividad and European Feder Funds (MAT2015-64139-C4-3-R, ENE2015-68320-R). The TEM measurements were performed in the Laboratorio de Microscopias Avanzadas (LMA) at the Instituto de Nanociencia de Aragon (INA) - Universidad de Zaragoza (Spain) and received funding from the European Union Seventh Framework Program under Grant Agreement 312483 - ESTEEM2 (Integrated Infrastructure Initiative - I3). B. Puértolas thanks the Ministry of Education for FPU grant (FPU grant AP2009-3544). A. Moragues thanks the Ministry of Economia y Competitividad for FPI grant (FPI grant BES2009-040029). UV is also acknowledged by the UV-INV-AE16-484416 project.

Appendix A. Supplementary material

Supplementary data associated with this article (CO conversion vs time for MCM-41 related catalysts, STEM-HAADF images of Ti-free Au/UVM-7 material, TEM and EDX mappings of Au-Ti5-UVM-7(2)RT, HRTEM images of Au-Ti5-UVM-7(2) calcined at 400 and 800ºC and ^{29}Si MAS NMR spectra) can be found, in the online version, at https://doi.org/....

References

1. M. Haruta, T. Kobayashi, H. Sano, N. Yamada, Novel gold catalysts for the oxidation of carbon-monoxide at a temperature far below 0ºC, Chem. Lett. 16 (1987) 405-408.

2. G. J. Hutchings, Vapor-phase hydrochlorination of acetylene - correlation of catalytic activity of supported metal chloride catalysts, J. Catal. 96 (1985) 292-295.
3. G. J. Hutchings, Nanocrystalline gold and gold palladium alloy catalysts for chemical synthesis, Chem. Comm. (2008) 1148-1164.
4. G. J. Hutchings, Heterogeneous catalysts-discovery and design, J. Mater. Chem. 19 (2009) 1222-1235.
5. M. Haruta, M. Date, Advances in the catalysis of au nanoparticles, Appl. Catal. A: General 222 (2001) 427-437.
6. G. C. Bond, D. T. Thompson, Catalysis by gold, Cat. Rev.-Sci. Eng. 41 (1999) 319-388.
7. B. K. Min, C. M. Friend, Heterogeneous gold-based catalysis for green chemistry: low-temperature co oxidation and propene oxidation, Chem. Rev. 107 (2007) 2709-2724.
8. M. Chen, D. W. Goodman, Catalytically active gold: from nanoparticles to ultrathin films, Acc. Chem. Res. 39 (2006) 739-746.
9. S. Scirè, L. F. Liotta, Supported gold catalysts for the total oxidation of volatile organic compounds, App. Catal. B: Environmental 125 (2012) 222-246.
10. A. Corma, H. Garcia, Supported gold nanoparticles as catalysts for organic reactions, Chem. Soc. Rev. 37 (2008) 2096-2126.
11. Y. Zhang, X. Cui, F. Shi, Y. Deng, Nano-gold catalysis in fine chemical synthesis. Chem. Rev. 112 (2012) 2467-2505.
12. A. Villa, N. Dimitratos, C. E. Chan-Thaw, C. Hammond, G. M. Veith, D. Wang, M. Manzoli, L. Prati, G. J. Hutchings, Characterisation of gold catalysts, Chem. Soc. Rev. 45 (2016) 4953-4994.
13. L.-W. Guo, P.-P. Du, X.-P. Fu, C. Ma, J. Zeng, R. Si, Y.-Y. Huang, C.-J. Jia, Y.-W. Zhang, C.-H. Yan, Contributions of distinct gold species to catalytic reactivity for carbon monoxide oxidation, Nature Communications 7 (2016) 13481.
14. L. Liu, Y. Gao, P. Zhao, X. Wang, G. Feng, R. Zhang, Pillared clay-supported gold catalysts for CO oxidation, RSC Adv. 6 (2016) 15121-15126.
15. R. Zanella, C. Louis, Influence of the conditions of thermal treatments and of storage on the size of the gold particles in Au/TiO_2 samples, Catal. Today 107-108 (2005) 768-777.
16. J. A. A. J. Perenboom, P. Wyder, F. Meier, Electronic properties of small metallic particles, Phys. Rep. 78 (1981) 173-292.

17. W. P. Halperin, Quantum size effects in metal particles, Rev. Mod. Phys. 58 (1986) 533-606.
18. M. B. Boucher, S. Goergen, N. Yi, M. Flytzani-Stephanopoulos, 'Shape effects' in metal oxide supported nanoscale gold catalysts, Phys. Chem. Chem. Phys. 13 (2011) 2517-2527.
19. A. M. Centeno, T. Ramírez Reina, S. Ivanova, H. O. Laguna, A. J. Odriozola, Au/CeO_2 catalysts: structure and CO oxidation activity, Catalysts 6 (2016) 158.
20. T. Akita, M. Kohyama, M. Haruta, Electron microscopy study of gold nanoparticles deposited on transition metal oxides, Acc.Chem. Res. 46 (2013) 1773-1782.
21. Z. Ma, S. Dai, Development of novel supported gold catalysts: a materials perspective, Nano Res. 4 (2011) 3-32.
22. J. Sun, X. Bao, Textural manipulation of mesoporous materials for hosting of metallic nanocatalysts, Chem. Eur. J. 14 (2008) 7478-7488.
23. L.-F. Gutiérrez, S. Hamoudi, K. Belkacemi, Synthesis of gold catalysts supported on mesoporous silica materials: recent developments, Catalysts 1 (2011) 97-154.
24. H. Wu, G. Pantaleo, M. A. Venezia, F. L. Liotta, Mesoporous silica based gold catalysts: novel synthesis and application in catalytic oxidation of CO and volatile organic compounds (VOCs), Catalysts 3 (2013) 774-793.
25. A. Beloqui Redondo, M. Ranocchiari, J. A. van Bokhoven, Synthesis of sub-nanometer gold particles on modified silica, Dalton Trans. 45 (2016) 2983-2988.
26. N. Ishito, K. Nakajima, Y. Maegawa, S. Inagaki, A. Fukuoka, Facile formation of gold nanoparticles on periodic mesoporous bipyridine-silica, Catal. Today 298 (2017) 258-262.
27. J. Luo, O. Ersen, W. Chu, T. Dintzer, P. Petit, C. Petit, Anchoring and promotion effects of metal oxides on silica supported catalytic gold nanoparticles, J. Coll. Inter. Sci. 482 (2016) 135-141.
28. X. Y. Liu, A. Wang, T. Zhang, C.-Y. Mou, Catalysis by gold: new insights into the support effect, Nano Today 8 (2013) 403-416.
29. N. Ta, J. Liu, S. Chenna, P. A. Crozier, Y. Li, A. Chen, W. Shen, Stabilized gold nanoparticles on ceria nanorods by strong interfacial anchoring, J. Am. Chem. Soc. 134 (2012) 20585-20588.
30. M. S. Scurrell, Thoughts on the use of gold-based catalysts in environmental protection catalysis, Gold Bull. 50 (2017) 77-84.

31. C. T. Campbell, S. C. Parker, D. E. Starr, The effect of size-dependent nanoparticle energetics on catalyst sintering, Science 298 (2002) 811-814.
32. S. H. Joo, J. Y. Park, C.-K. Tsung, Y. Yamada, P. Yang, G. A. Somorjai, Thermally stable pt/mesoporous silica core-shell nanocatalysts for high-temperature reactions, Nature Mater. 8 (2009) 126-131.
33. A. J. Zarur, J. Y. Ying, Reverse microemulsion synthesis of nanostructured complex oxides for catalytic combustion, Nature 403 (2000) 65-67.
34. H. S. Gandhi, G. W. Graham, R. W. McCabe, Automotive exhaust catalysis, J. Catal. 216 (2003) 433-442.
35. H. Zhu, Z. Ma, S. H. Overbury, S. Dai, Rational design of gold catalysts with enhanced thermal stability: post modification of Au/TiO_2 by amorphous SiO_2 decoration, Catal. Lett. 116 (2007) 128-135.
36. P. M. Arnal, M. Comotti, F. Schüth, High-temperature-stable catalysts by hollow sphere encapsulation, Angew. Chem. Int. Ed. 45 (2006) 8224-8227.
37. C. Chen, M. Shi, M. Cargnello, P. Fornasiero, C. B. Murray, R. J. Gorte, $Au@TiO_2$ core-shell nanostructures with high thermal stability, Catal. Lett. 144 (2014) 1939-1945.
38. K. Zhao, B. Qiao, J. Wang, Y. Zhang, T. Zhang, A highly active and sintering-resistant Au/FeO_x-hydroxyapatite catalyst for CO oxidation, Chem. Comm. 47 (2011) 1779-1781.
39. J. Wang, A.-H. Lu, M. Li, W. Zhang, Y.-S. Chen, D.-X. Tian, W.-C. Li, Thin porous alumina sheets as supports for stabilizing gold nanoparticles, ACS Nano 7 (2013) 4902-4910.
40. J. R. Mellor, A. N. Palazov, B. S. Grigorova, J. F. Greyling, K. Reddy, M. P. Letsoalo, J. H. Marsh, The application of supported gold catalysts to automotive pollution abatement, Catal. Today 72 (2002) 145-156.
41. EP 1 043 059 Patent to Toyota Jidosha Kabushiki Kaisha Toyota, 11 Oct. 2000.
42. R. Köhn, M. Fröba, Nanoparticles of 3d transition metal oxides in mesoporous MCM-48 silica host structures: synthesis and characterization, Catal. Today 68 (2001) 227-236.
43. G. J. D. Soler-illia, C. Sanchez, B. Lebeau, J. Patarin, Chemical strategies to design textured materials: from microporous and mesoporous oxides to nanonetworks and hierarchical structures, Chem. Rev. 102 (2002) 4093-4138.
44. Z. Liu, R. Che, A. A. Elzatahry, D. Zhao, Direct imaging Au Nanoparticle migration inside mesoporous silica channels, ACS Nano 8 (2014) 10455-10460.

45. B. Puertolas, A. Mayoral, R. Arenal, B. Solsona, A. Moragues, S. Murcia-Mascaros, P. Amoros, A. B. Hungria, S. H. Taylor, T. Garcia, High-temperature stable gold nanoparticle catalysts for application under severe conditions: the role of TiO_2 nanodomains in structure and activity, ACS Catal. 5 (2015) 1078-1086.
46. J. El Haskouri, D. O. de Zarate, C. Guillem, J. Latorre, M. Caldes, A. Beltran, D. Beltran, A. B. Descalzo, G. Rodriguez-Lopez, R. Martinez-Manez, M. D. Marcos, P. Amoros, Silica-based powders and monoliths with bimodal pore systems, Chem. Comm. (2002) 330-331.
47. J. El Haskouri, J. M. Morales, D. O. de Zarate, L. Fernandez, J. Latorre, C. Guillem, A. Beltran, D. Beltran, P. Amoros, Nanoparticulated silicas with bimodal porosity: chemical control of the pore sizes, Inorg. Chem. 47 (2008) 8267-8277.
48. M. Perez-Cabero, A. B. Hungria, J. M. Morales, M. Tortajada, D. Ramon, A. Moragues, J. El Haskouri, A. Beltran, D. Beltran, P. Amoros, Interconnected mesopores and high accessibility in UVM-7-like silicas, J. Nanopart. Res. 14 (2012) 12.
49. S. Cabrera, J. El Haskouri, C. Guillem, J. Latorre, A. Beltran, D. Beltran, M. D. Marcos, P. Amoros, Generalised syntheses of ordered mesoporous oxides: the atrane route, Solid State Sci. 2 (2000) 405-420.
50. J. El Haskouri, D. O. de Zarate, F. Perez-Pla, A. Cervilla, C. Guillem, J. Latorre, M. D. Marcos, A. Beltran, D. Beltran, P. Amoros, Improving epoxide production using Ti-UVM-7 porous nanosized catalysts, New J. Chem. 26 (2002) 1093-1095.
51. V. S. Narkhede, A. De Toni, V. V. Narkhede, M. Guraya, J. W. Niemantsverdriet, M. W. E. van den Berg, W. Gruenert, H. Gies, Au/TiO_2 catalysts encapsulated in the mesopores of siliceous MCM-48 -reproducible synthesis, structural characterization and activity for CO oxidation, Microp. Mesop. Mater. 118 (2009) 52-60.
52. M. Haruta, S. Tsubota, T. Kobayashi, H. Kageyama, M. J. Genet, B. Delmon, Low-temperature oxidation of CO over gold supported on TiO_2, alpha-Fe_2O_3, and Co_3O_4, J. Catal. 144 (1993) 175-192.
53. C. Jeanguillaume, C. Colliex, Spectrum-image - the next step in EELS Digital acquisition and processing, Ultramicroscopy 28 (1989) 252-257.
54. R. Arenal, F. de la Pena, O. Stephan, M. Walls, M. Tence, A. Loiseau, C. Colliex, Extending the analysis of EELS spectrum-imaging data, from elemental to bond mapping in complex nanostructures, Ultramicroscopy 109 (2008) 32-38.

55. R. K. Iller, The Chemistry of Silica. Solubilty, Polimerization, Colloid and Surface Properties and Biochemistry. John Wiley & Sons. New York, 1979.
56. M. Okumura, T. Fujitani, J. Huang, T. Ishida, A Career in Catalysis: Masatake Haruta, ACS Catal. 5 (2015) 4699-4707.
57. C. F. Baes, R. E. Mesmer, The Hydrolysis of Cations. John Wiley & Sons. New York, 1976.
58. M. Zhang, L. Shi, S. Yuan, Y. Zhao, J. Fang, Synthesis and photocatalytic properties of highly stable and neutral TiO_2/SiO_2 hydrosol, J. Coll. Inter. Sci. 330 (2009) 113-118.
59. F. Moreau, G. C. Bond, A. O. Taylor, Gold on titania catalysts for the oxidation of carbon monoxide: control of pH during preparation with various gold contents, J. Catal. 231 (2005) 105-114.
60. F. Moreau, G. C. Bond, Preparation and reactivation of Au/TiO_2 catalysts, Catal. Today 122 (2007) 260-265.
61. V. I. Parvulescu, S. M. Coman, N. Candu, J. El Haskouri, D. Beltran, P. Amoros, Synthesis, characterization and catalytic behavior of SnTf/MCM-41 and SnTf/UVM-7 as new green catalysts for etherification reactions, J. Mater. Sci. 44 (2009) 6693-6700.
62. S. Schacht, M. Janicke, F. Schüth, Modeling X-ray patterns and TEM images of MCM-41, Microp. Mesop. Mater. 22 (1998) 485-493.
63. J. A. Moulijn, A. E. van Diepen, F. Kapteijn, Catalyst deactivation: is it predictable? What to do? App. Catal. A:General 212 (2001) 3-16.
64. C. T. Kresge, M. E. Leonowicz, W. J. Roth, J. C. Vartuli, J. S. Beck, Ordered mesoporous molecular-sieves synthesized by a liquid-crystal template mechanism, Nature 359 (1992) 710-712.
65. K.-R. Zhu, M.-S. Zhang, Q. Chen, Z. Yin, Size and phonon-confinement effects on low-frequency raman mode of anatase TiO_2 nanocrystal, Phys. Lett. A 340 (2005) 220-227.
66. S. Kelly, F. H. Pollak, M. Tomkiewicz, Raman spectroscopy as a morphological probe for TiO_2 aerogels, J. Phys. Chem. B 101 (1997) 2730-2734.
67. Z. Luan, E. M. Maes, P. A. W. van der Heide, D. Zhao, R. S. Czernuszewicz, L Kevan, Incorporation of titanium into mesoporous silica molecular sieve SBA-15, Chem. Mater. 11 (1999) 3680-3686.
68. S. Wang, Y. Shi, X. Ma, Microwave synthesis, characterization and transesterification activities of Ti-MCM-41, Microp. Mesop. Mater. 156 (2012) 22-28.

69. Y. Su, M. L. Balmer, B. C. Bunker, Raman spectroscopic studies of silicotitanates, J. Phys. Chem. B 104 (2000) 8160-8169.
70. M. D. Alba, Z. Luan, J. Klinowski, Titanosilicate mesoporous molecular sieve MCM-41: synthesis and characterization, J. Phys. Chem. 100 (1996) 2178-2182.
71. A. Labouriau, T. J. Higley, W. L. Earl, Chemical shift prediction in the Si^{29} MAS NMR of titanosilicates, J. Phys. Chem. B 102 (1998) 2897-2904.
72. J. M. Morales, A. Moragues, J. El Haskouri, C. Guillem, J. Latorre, S. Murcia-Mascarós, A. Beltrán, D. Beltrán, P. Amorós, Low-cost synthesis of bimodal mesoporous silica-based materials by pseudomorphic transformation, ChemPlusChem 80 (2015) 1014-1028.

Table 1

Selected synthetic and physical data for Ti-UVM-7 and TiO_2/UVM-7 porous supports.

	Sample	Si/Ti[a]	Si/Ti[b]	Si/Au[b]	S_{BET} / m^2g^{-1}
	UVM-7	-	-	-	1140
Ti-UVM-7 or Au/Ti-UVM-7	Ti21-UVM-7(1)RT	21	13	-	1024
	Ti5-UVM-7(1)RT	5	5	-	1115
	Ti4-UVM-7(1)RT	4	3	-	742
	Ti1-UVM-7(1)RT	1	0.8	-	2
	Au-Ti21-UVM-7(1)RT	21	14	57	1044
	Au-Ti5-UVM-7(1)RT	5	4	28	747
	Au-Ti4-UVM-7(1)RT	4	3	38	560
	Au-Ti1-UVM-7(1)RT	1	1.1	59	1
TiO_2/UVM-7 or Au/TiO_2/UVM-7	Ti21-UVM-7(2)RT	21	25	-	1030
	Ti5-UVM-7(2)RT	5	10	-	931
	Ti4-UVM-7(2)RT	4	6	-	912
	Ti1-UVM-7(2)RT	1	2	-	23
	Au-Ti21-UVM-7(2)RT	21	17	27	928
	Au-Ti5-UVM-7(2)RT	5	4	20	846
	Au-Ti4-UVM-7(2)RT	4	3	30	779
	Au-Ti1-UVM-7(2)RT	1	1	75	12

[a] Si/Ti molar ratio in the mother liquor (before or after the gold incorporation). [b] Si/Ti and Si/Au molar ratio values from EDX.

Table 2

Physical data for uncalcined and calcined catalysts.

	Sample	Surface[a] / m^2/g	Intra-particle mesopore system / $P/P_0<0.7$ Size[b] / nm	Intra-particle mesopore system / $P/P_0<0.7$ Volume[b] / cm^3/g	Inter-particle pore system / $P/P_0>0.7$ Size[b] / nm	Inter-particle pore system / $P/P_0>0.7$ Volume[b] / cm^3/g
Ti-UVM-7 or Au/Ti-UVM-7	Ti5-UVM-7(1)RT	1115	2.52	0.82	41.23	0.98
	Au-Ti5-UVM-7(1)RT	747	2.46	0.48	42.00	0.54
	Au-Ti5-UVM-7(1)400	458	2.45	0.47	41.35	0.58
	Au-Ti5-UVM-7(1)800	55	< 2	0.04	21.39	0.46
TiO_2/UVM-7 or Au/TiO_2/UVM-7	Ti5-UVM-7(2)RT	931	2.81	0.79	25.50	1.28
	Au-Ti5-UVM-7(2)RT	846	2.61	0.66	35.10	1.30
	Au-Ti5-UVM-7(2)400	632	2.58	0.54	33.21	0.99
	Au-Ti5-UVM-7(2)800	245	< 2	0.18	24.37	0.55

[a] Surface area according to the BET model.

[b]Pore diameters and volumes calculated by using the BJH model on the adsorption branch of the isotherms.

Table 3

^{29}Si NMR data from the spectra deconvolution.

	Q^4		Q^3 and/or Si(3Si,1Ti)		Q^2 and/or Si(2Si,2Ti)	
	δ / ppm	%	δ / ppm	%	δ / ppm	%
UVM-7(800)	-114	76	-104	23	-95	1
Au-Ti5-UVM-7(2)800	-111	71	-102	26	-93	3
Au-Ti5-UVM-7(1)RT	-110	64	-101	32	-93	4
Au-Ti5-UVM-7(1)800	-110	61	-101	30	-94	3

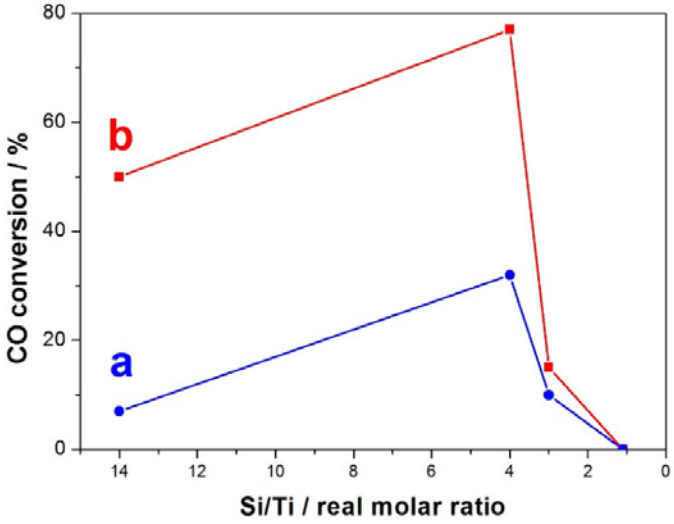

Figure 1. CO conversion values *vs.* Si/Ti (real molar ratio) for uncalcined catalysts after 2 days time-on-line for (a) Au-Tix-UVM-7(1)RT and (b) Au-Tix-UVM-7(2)RT catalysts. Conditions: 0.4%v/v CO, 20% v/v O_2 and argon balance, space velocity = 600000 $cm^3/(gcat \cdot h)$, reaction temperature = 20 ºC.

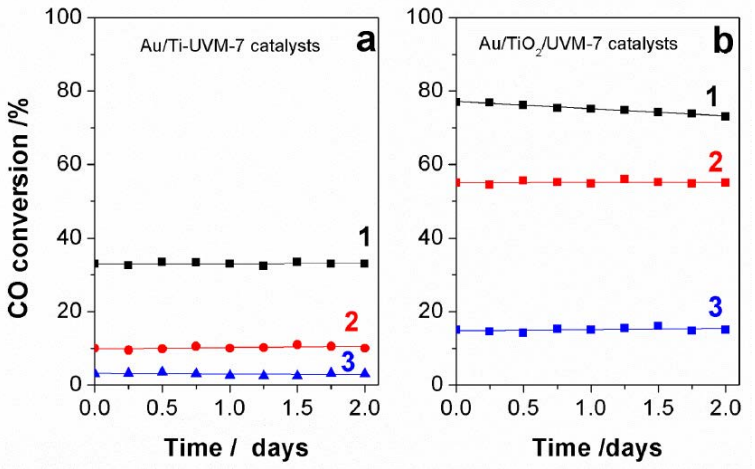

Figure 2. CO conversion vs. time for catalysts prepared through (a) the Atrane *one pot* method ((1) Au-Ti5-UVM-7(1)RT, (2) Au-Ti5-UVM-7(1)400 and (3) Au-Ti5-UVM-7(1)800, and (b) the *two-pot* strategy ((1) Au-Ti5-UVM-7(2)RT, (2) Au-Ti5-UVM-7(2)400 and (3) Au-Ti5-UVM-7(2)800). Conditions: 0.4% v/v CO, 20% v/v O_2 and argon balance, space velocity = 600000 $cm^3/(g\ cat \cdot h)$, reaction temperature = 20 ºC.

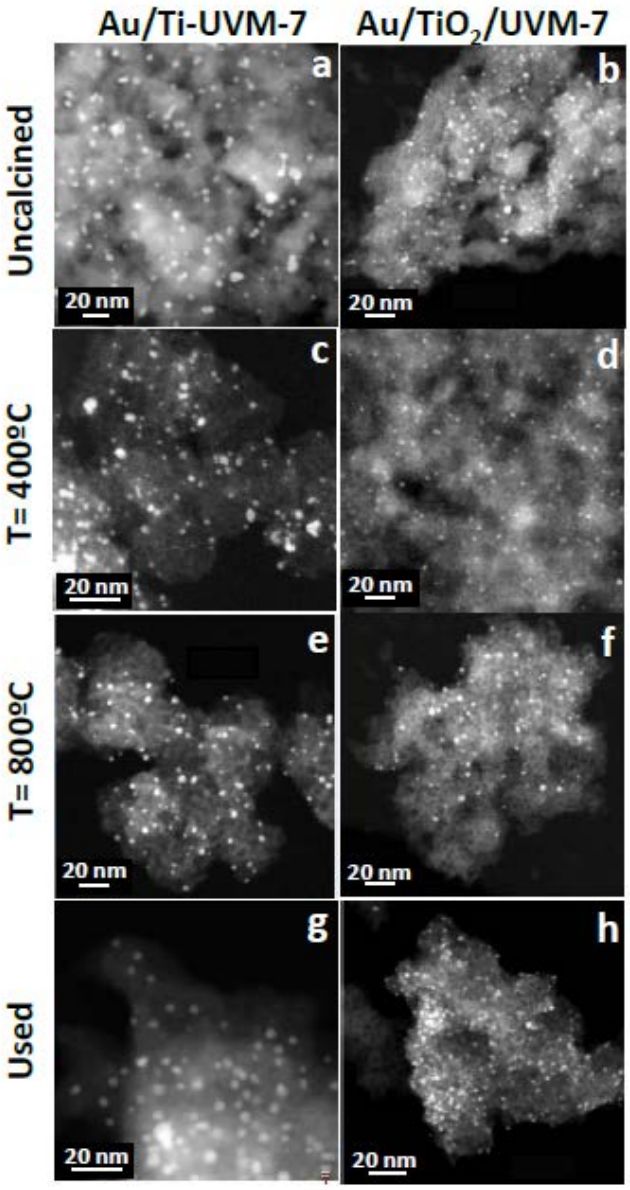

Figure 3. STEM-HAADF images of (a) Au-Ti5-UVM-7(1)RT, (b) Au-Ti5-UVM-7(2)RT, (c) Au-Ti5-UVM-7(1)400, (d) Au-Ti5-UVM-7(2)400, (e) Au-Ti5-UVM-7(1)800, (f) Au-Ti5-UVM-7(2)800, (g) Au-Ti5-UVM-7(1)800 used and (h) Au-Ti5-UVM-7(2)800 used.

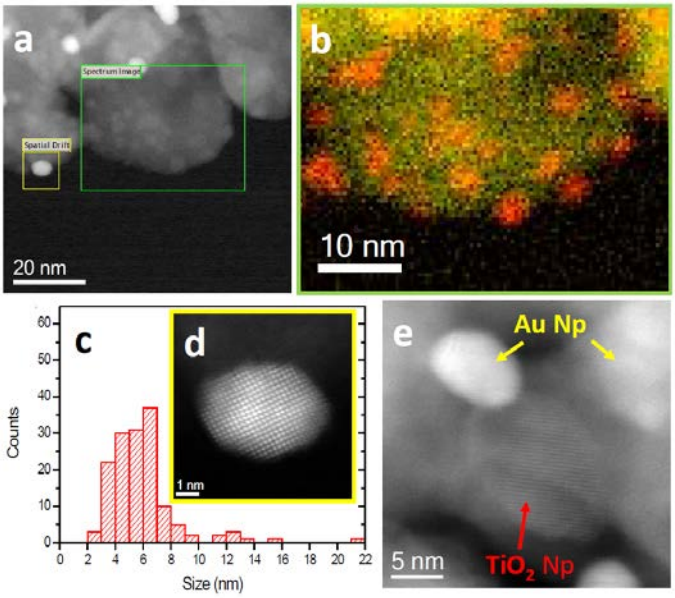

Figure 4. (a) Cs-corrected STEM-HAADF images of the Au-Ti5-UVM-7(1)RT. (b) Ti-L3,2 (red) and O-K (yellow) maps superimposed on the HRSTEM-HAADF image. (c) Gold nanoparticle size distribution. (d) High magnification image of a gold nanoparticle. (e) High magnification image where the TiO_2 nanoparticles are identified together with the Au nanoparticles.

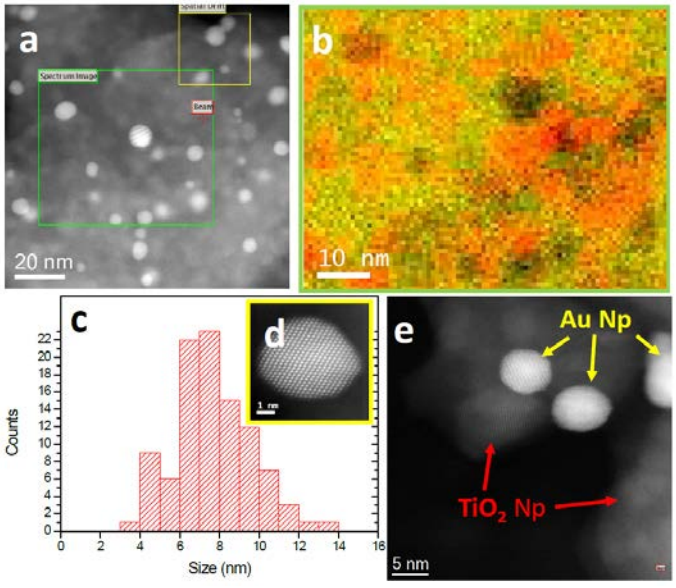

Figure 5. (a) Cs-corrected STEM-HAADF images of the Au-Ti5/UVM-7(1)800. (b) Ti-L3,2 (red) and O-K (yellow) maps superimposed on the HRSTEM-HAADF image. (c) Gold nanoparticle size distribution. (d) High magnification image of a gold nanoparticle. (e) High magnification image where the TiO_2 nanoparticles are identified together with the Au nanoparticles.

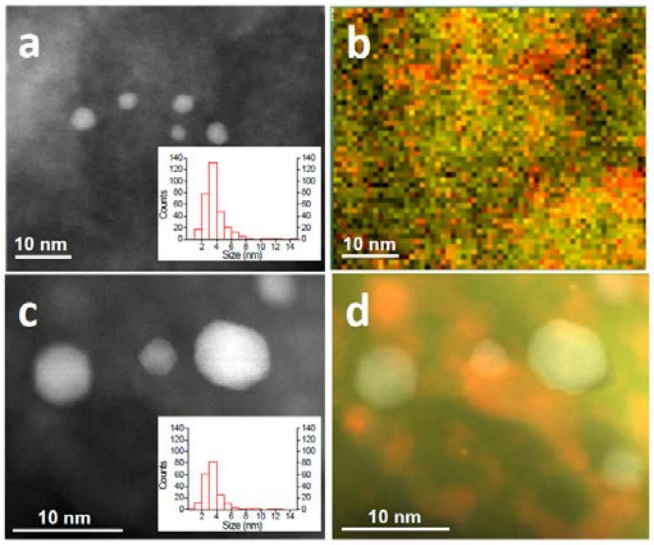

Figure 6. (a) Cs-corrected STEM-HAADF image and (b) Ti-L3,2 (red) and O-K (yellow) maps of the Au-Ti5-UVM-7(2)RT. (c) Cs-corrected STEM-HAADF image and (d) Ti-L3,2 (red) and O-K (yellow) maps of the Au-Ti5-UVM-7(2)800. In the insets the respective gold nanoparticle size distribution have been presented.

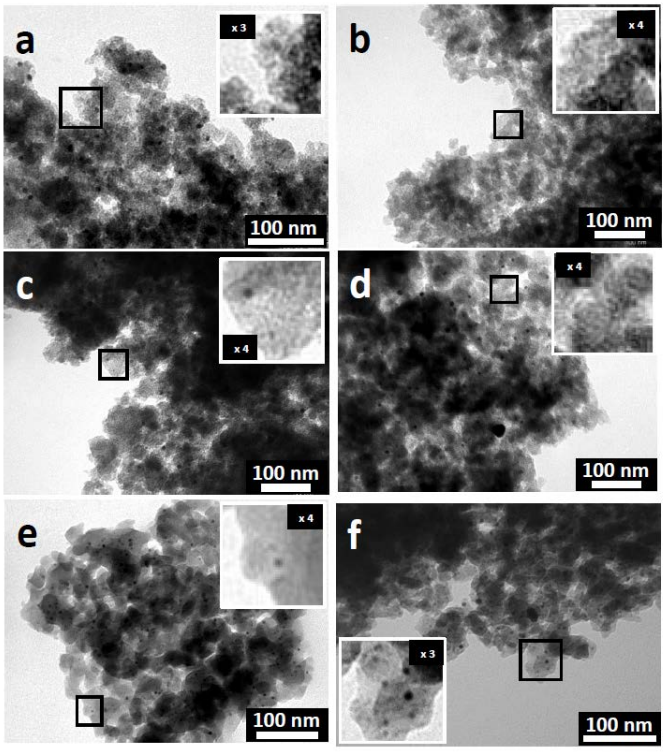

Figure 7. TEM images of (a) Au-Ti5-UVM-7(1)RT, (b) Au-Ti5-UVM-7(2)RT, (c) Au-Ti5-UVM-7(1)400, (d) Au-Ti5-UVM-7(2)400, (e) Au-Ti5-UVM-7(1)800 and (f) Au-Ti5-UVM-7(2)800.

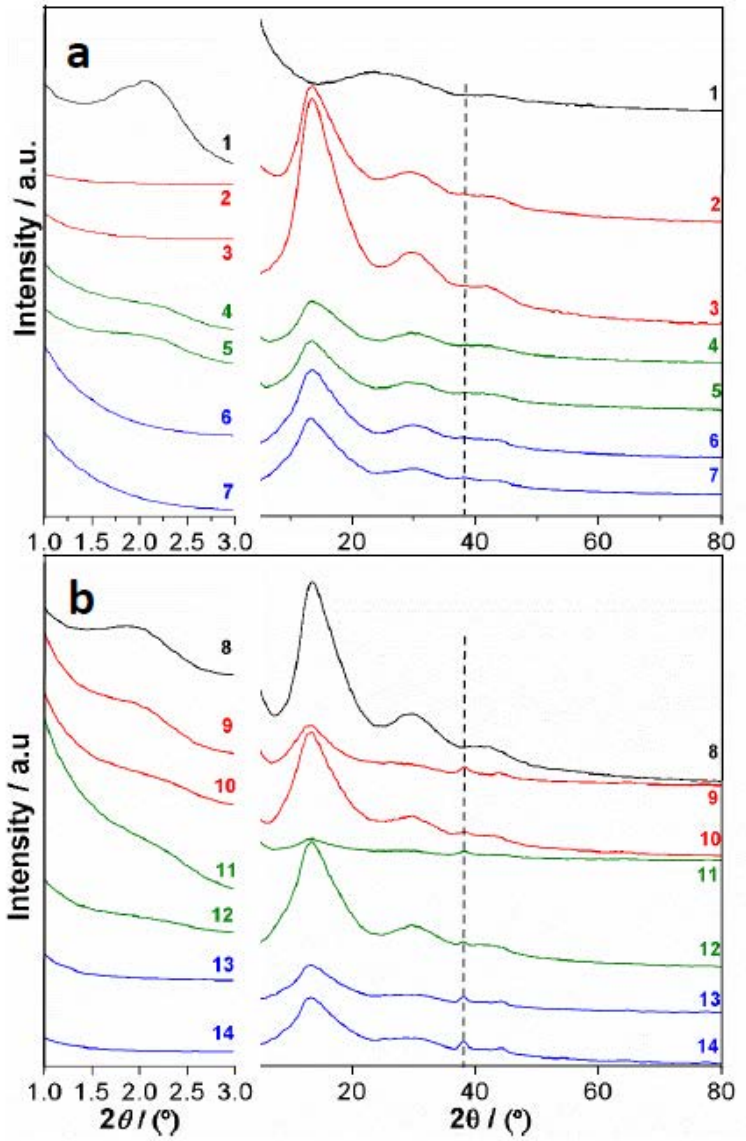

Figure 8. Low and high-angle XRD patterns of (a) Au/Ti-UVM-7 and (b) Au/TiO2/UVM-7 catalysts. (1) Ti5-UVM-7(1)RT. (2) Au-Ti5-UVM-7(1)RT. (3) Au-Ti5-UVM-7(1)RT used. (4) Au-Ti5-UVM-7(1)400. (5) Au-Ti5-UVM-7(1)400 used. (6) Au-Ti5-UVM-7(1)800. (7) Au-Ti5-UVM-7(1)800 used. (8) Ti5-UVM-7(2)RT. (9) Au-Ti5-UVM-7(2)RT. (10) Au-Ti5-UVM-7(2)RT used. (11) Au-Ti5-UVM-7(2)400. (12) Au-Ti5-UVM-7(2)400 used. (13) Au-Ti5-UVM-7(2)800. (14) Au-Ti5-UVM-7(2)800 used.

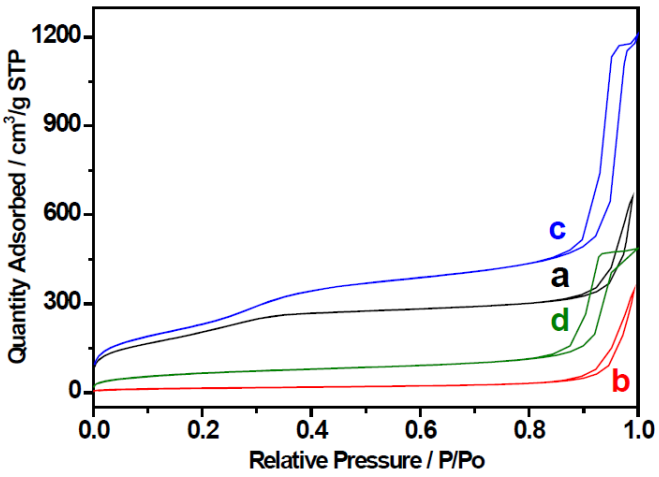

Figure 9. N_2 adsorption-desorption isotherms of (a) Au-Ti5-UVM-7(1)RT, (b) Au-Ti5-UVM-7(1)800, (c) Au-Ti5-UVM-7(2)RT and (d) Au-Ti5-UVM-7(2)800 catalysts. Isotherms have been y-shifted for clarity.

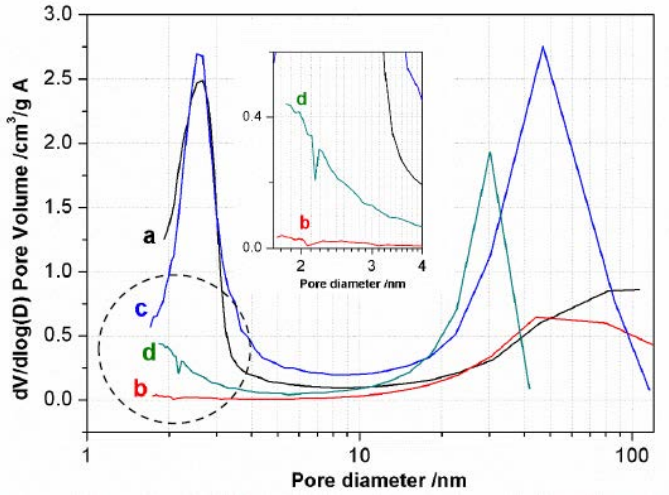

Figure 10. BJH pore size distributions of (a) Au-Ti5-UVM-7(1)RT, (b) Au-Ti5-UVM-7(1)800, (c) Au-Ti5-UVM-7(2)RT and (d) Au-Ti5-UVM-7(2)800 catalysts.

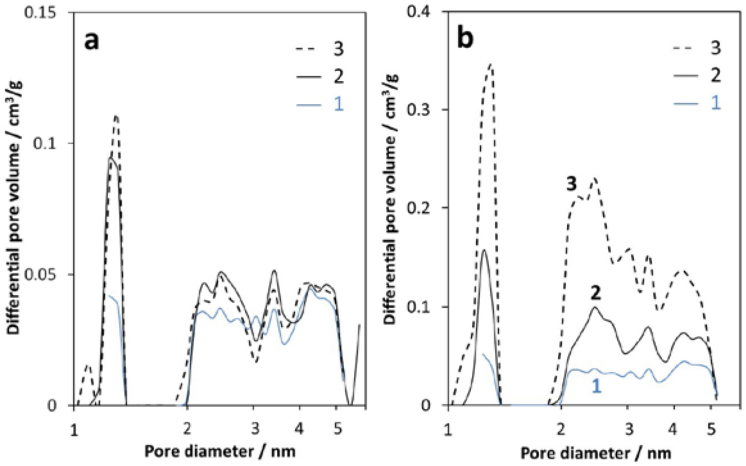

Figure 11. DFT pore size distributions of (a) catalysts prepared through the Atrane route ((1) UVM-7 800; (2) Ti5-UVM-7(1)800; (3) Au-Ti5-UVM-7(1)800), and (b) catalyst prepared by the *two-pot* route ((1) UVM-7 800; (2) Ti5-UVM-7(2)800; (3) Au-Ti5-UVM-7(2)800).

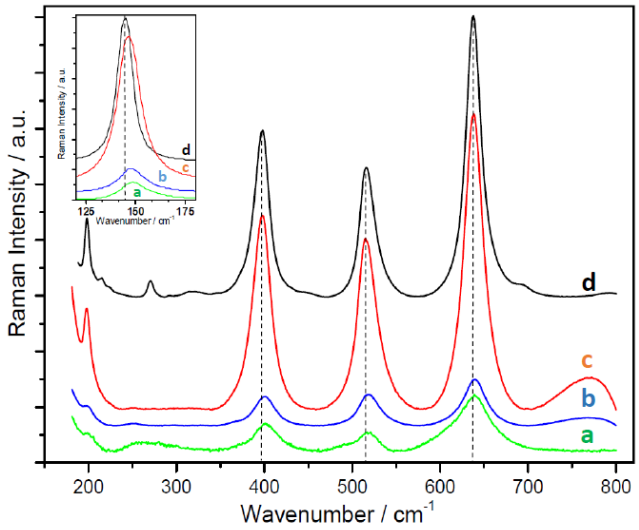

Figure 12. Raman spectra of Ti-Si supports (a) Ti5-UVM-7(2)RT, (b) Ti5-UVM-7(2)400, (c) Ti5-UVM-7(2)800 and (d) anatase (as reference). In the inset we show the spectral zone where the intense anatase signal appears.

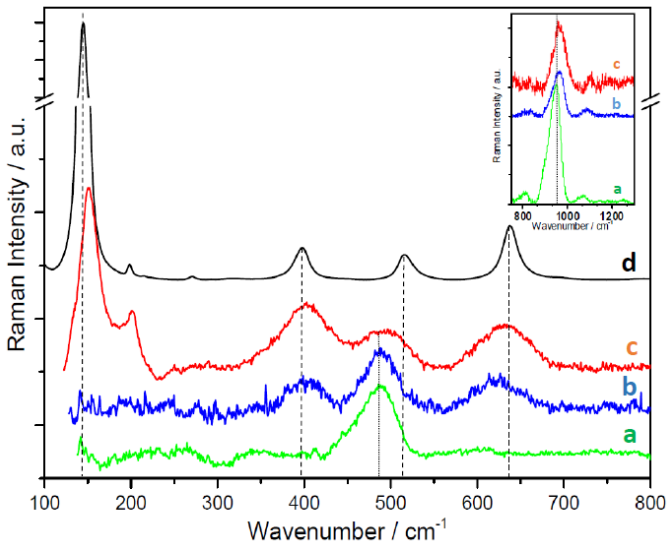

Figure 13. Raman spectra of Ti-Si supports (a) Ti5-UVM-7(1)RT, (b) Ti5-UVM-7(1)400, (c) Ti5-UVM-7(1)800 and (d) anatase (as reference). In the inset we show the spectral zone where Si-O-Ti signals appears.

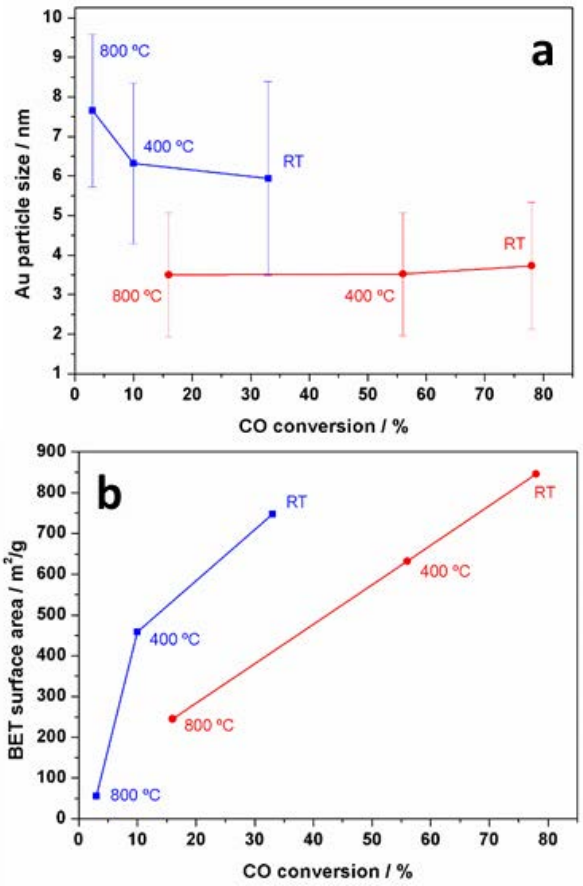

Figure 14. Evolution of the CO conversion with (a) the gold nanoparticle size, and (b) the BET surface area. ■ Au-Ti5-UVM-7(1)CT. ● Au-Ti5-UVM-7(2)CT. CT= RT, 400ºC, 800ºC.

Appendix A. Supplementary material

Understanding the role of Ti-rich domains in the stabilization of gold nanoparticles on mesoporous silica-based catalysts

Alaina Moragues [a], Begoña Puértolas [b], Álvaro Mayoral [c,d], Raúl Arenal [c,d], Ana B. Hungría [e], Sonia Murcia-Mascarós [a], Stuart H. Taylor [f], Benjamín Solsona [g,*], Tomás García[b,*], Pedro Amorós [a,*]

[a] Institut de Ciència dels Materials, Universitat de València, P.O. Box 22085, 46071 Valencia, Spain.

[b] Instituto de Carboquímica (ICB-CSIC), C/ Miguel Luesma Castán 4, 50018 Zaragoza, Spain.

[c] Laboratorio de Microscopias Avanzadas (LMA), Instituto de Nanociencia de Aragon (INA), Universidad de Zaragoza, Mariano Esquillor, 50018 Zaragoza, Spain.

[d] Fundación Agencia Aragonesa para la Investigación y el Desarrollo (ARAID), María de Luna 11, 50018 Zaragoza, Spain.

[e] Departamento de Ciencia de Materiales, Ingeniería Metalúrgica y Química Inorgánica, Universidad de Cádiz, Campus Río San Pedro, 11510 Puerto Real, Spain.

[f] Cardiff Catalysis Institute, School of Chemistry, Cardiff University, Main Building, Park Place, CF10 3AT Cardiff, United Kingdom.

[g] Departamento de Ingenieria Quimica, Universitat de València, Avenida de la Universitat, 46071 Valencia, Spain.

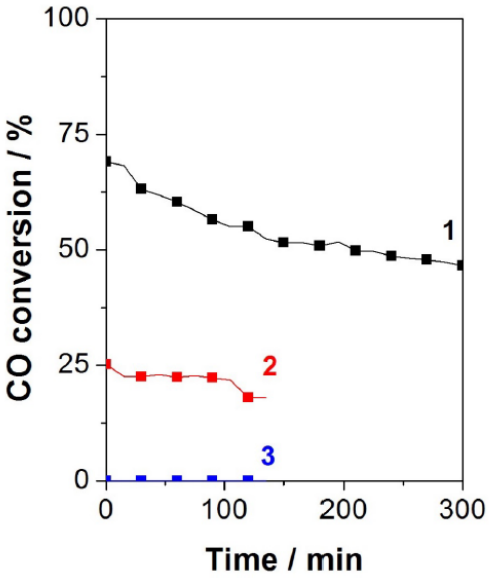

Figure S1. CO conversion vs. time for catalysts prepared through the *two-pot* strategy ((1) Au-Ti6-MCM-41(2)RT, (2) Au-Ti6-MCM-41(2)400 and (3) Au-Ti6-MCM-41(2)800).

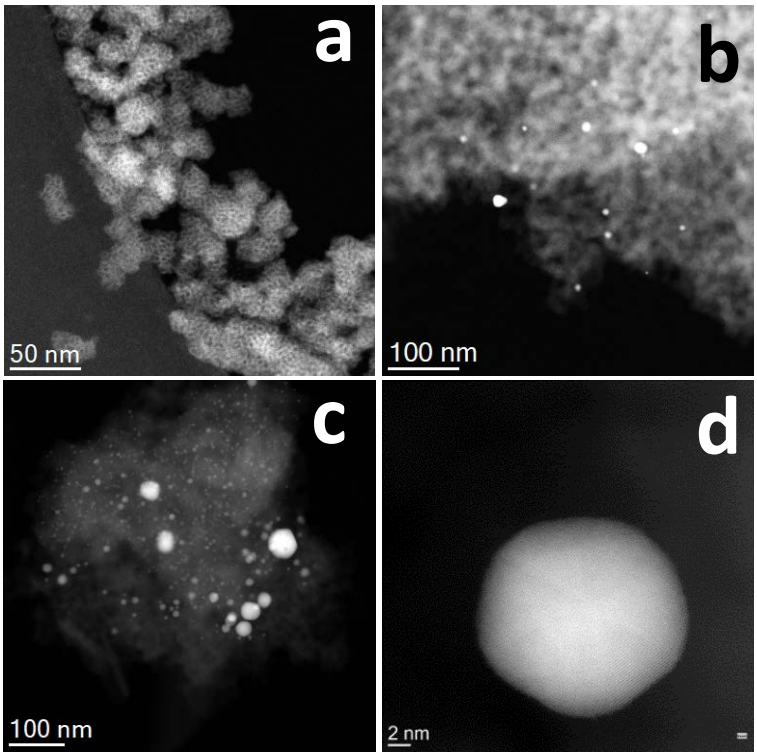

Figure S2. STEM-HAADF images of Au/UVM-7. (a, b) uncalcined catalyst. (c, d) catalyst calcined at 800ºC.

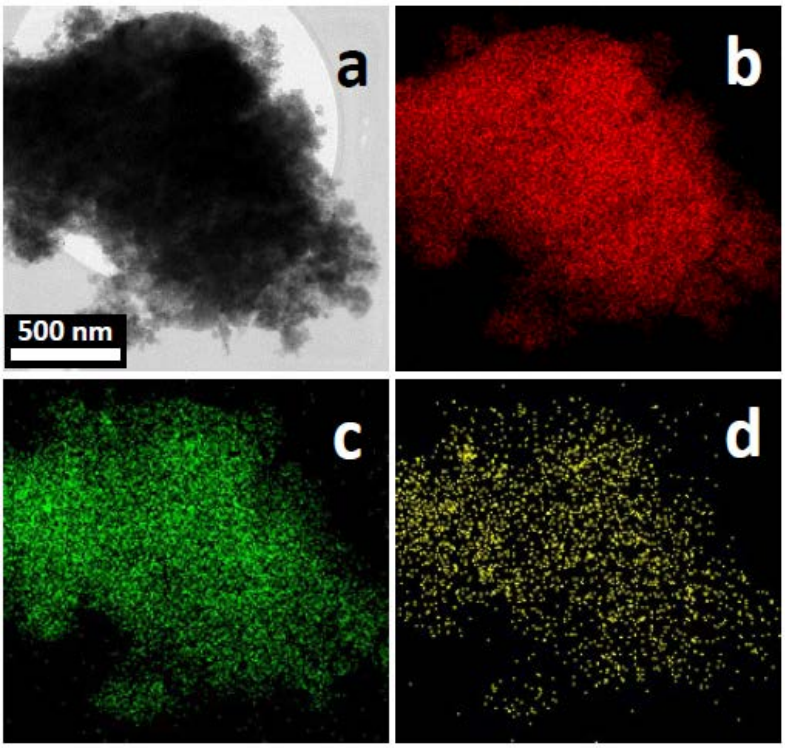

Figure S3. TEM image (a) and EDX mapping of Au-Ti5-UVM-7(2)RT catalyst. (b) Si distribution. (c) Ti distribution. (c) Au distribution.

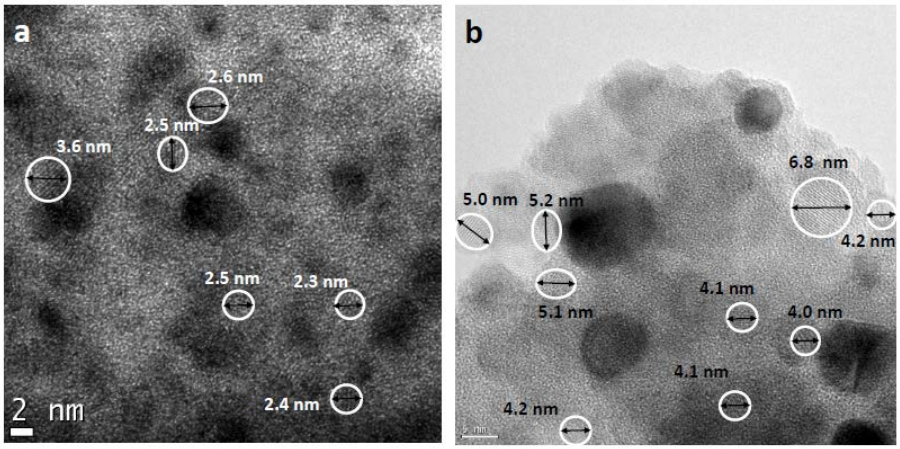

Figure S4. HRTEM image of (a) Au-Ti5-UVM-7(2)400 and (a) Au-Ti5-UVM-7(2)800.

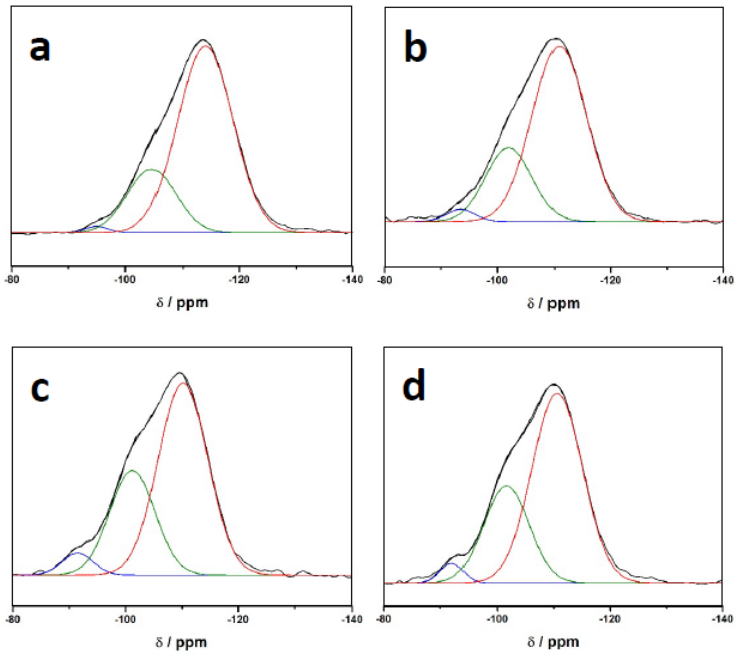

Figure S5. ^{29}Si NMR spectra of (a) UVM-7 pure silica calcined at 800ºC, (b) Au-Ti5-UVM-7(2)800, (c) Au-Ti5-UVM-7(1)RT and (d) Au-Ti5-UVM-7(1)800. Blue, green and red Gaussian curves correspond to Q^2 (or Si(2Si,2Ti), Q^3 (or Si(3Si,1Ti) and Q^4 sites, respectively.